

# Aging-Driven Composition and Distribution Changes of Electrolyte and Graphite Anode in 18650-Type Li-Ion Batteries

Dominik Petz, Volodymyr Baran, Christoph Peschel, Martin Winter, Sascha Nowak, Michael Hofmann, Robert Kostecki, Rainer Niewa, Michael Bauer, Peter Müller-Buschbaum, and Anatoliy Senyshyn\*

A series of low-temperature studies on  $\text{LiNi}_{0.80}\text{Co}_{0.15}\text{Al}_{0.05}\text{O}_2$  18650-type batteries of high-energy type with different stabilized states of fatigue is carried out using spatially resolved neutron powder diffraction, infrared/thermal imaging, and quasi-adiabatic calorimetry. In-plane distribution of lithium in the graphite anode and frozen electrolyte in fully charged state is determined non-destructively with neutron diffraction and correlated to the introduced state of fatigue. An independent electrolyte characterization is performed via calorimetry studies on variously aged 18650-type lithium-ion batteries, where the shape of the thermodynamic signal is evolving with the state of fatigue of the cells. Analyzing the liquid electrolyte extracted/harvested from the studied cells reveals the decomposition of conducting salt to be the main driving factor for fatigue in the electrolyte degradation.

in the segment of energy storage for portable electronics and electric drivetrains. Despite its overall popularity and widespread adoption resulting in extended development, the Li-ion technology still possesses a sufficient potential for improvement, especially in the aspects concerning assessing higher power and energy densities, minimization of power fading, increase of safety, etc.

Lithium-ion batteries (and also metal-ion batteries in general) are the subject of very intense research, where among the different components of metal-ion batteries, the electrolyte (either liquid or solid-state) remains the least characterized under operando conditions.<sup>[1]</sup> However,

the electrolyte is believed to be a key factor defining battery safety, lifetime, and temperature stability, as well as limitations on the applicability of high-voltage cathodes.<sup>[2]</sup> The development of a better understanding of electrolytes in addition to the perspective of using lithium metal anodes in all-solid-state batteries is actively pursued at the moment. However, the best cycling stability and performance is today achieved with quasi-solid-state-electrolytes consisting of a liquid electrolyte and a rigid framework either of inorganic or polymeric type.<sup>[3]</sup>


Most works in this area are dedicated to the tuning of the electrolyte composition toward improvement of the battery performance.<sup>[4,5]</sup> Different tuning approaches and strategies

## 1. Introduction

Energy storage is one of the key important challenges facing our society in the 21st century. Our daily life is directly related with the development and evolving of electrochemical energy storage systems, starting from Volta cells over lead-acid batteries to complex hybrid storage solutions explored nowadays. Lithium-ion batteries contributed remarkably to the societal changes and underwent a rapid development since their commercialization in 1991. Their outstanding energy and power densities, compared to other electrochemical energy storage systems available at the market, put Li-ion batteries dominating

D. Petz, V. Baran, M. Hofmann, P. Müller-Buschbaum, A. Senyshyn  
Forschungs-Neutronenquelle Heinz Maier-Leibnitz FRM II  
Technische Universität München  
Lichtenbergstr. 1, 85748 Garching bei München, Germany  
E-mail: Anatoliy.Senyshyn@frm2.tum.de

D. Petz, P. Müller-Buschbaum  
Lehrstuhl für Funktionelle Materialien, Physik-Department  
Technische Universität München  
James-Franck-Straße 1, 85748 Garching bei München, Germany

 The ORCID identification number(s) for the author(s) of this article can be found under <https://doi.org/10.1002/aenm.202201652>.

© 2022 The Authors. Advanced Energy Materials published by Wiley-VCH GmbH. This is an open access article under the terms of the Creative Commons Attribution License, which permits use, distribution and reproduction in any medium, provided the original work is properly cited.

DOI: 10.1002/aenm.202201652

V. Baran  
Deutsches Elektronen Synchrotron (DESY)  
Notkestr. 85, 22607 Hamburg, Germany

C. Peschel, M. Winter, S. Nowak  
Münster Electrochemical Energy Technology (MEET)  
Westfälische Wilhelms-Universität Münster  
Correnstr. 46, 48149 Münster, Germany

R. Kostecki  
Energy Storage and Distributed Resources Division  
Lawrence Berkeley National Laboratory  
Berkeley, CA 94720, USA

R. Niewa  
Institute of Inorganic Chemistry  
University of Stuttgart  
Pfaffenwaldring 55, 70569 Stuttgart, Germany

M. Bauer  
Department of Physics and Atmospheric Science  
Dalhousie University  
Halifax, NS B3H 3J5, Canada

are developed along with theoretical models of the degradation mechanisms involving the electrolyte.<sup>[6]</sup> However, the complexity of real cells and the number of various side reactions result in a unique degradation scenario for each cell chemistry and from cell to cell itself.<sup>[7,8]</sup> The majority of studies are carried out under post-mortem conditions, which for certain techniques is a non-alternative approach. Indeed, an accurate qualitative and quantitative description of the electrolyte under operando conditions is by far not trivial.

For example, the electrolyte in Li-ion batteries can be consumed for reactions on the anode or cathode surface or alternatively decomposed at high temperatures during active cycling. Quantification of its chemical composition and/or additives typically requires cell opening and electrolyte harvesting with centrifugation and further mass-spectroscopy, etc. Alternatively, it was shown recently that the amount of electrolyte can be accurately and non-destructively quantified using neutron diffraction in frozen state, where even a mm-sized resolved localization in cylindrical 18650-type cells was achieved.<sup>[9,10]</sup> It is worth to be mentioned that neutron-based experiments have a unique stance in battery research, where the low incident energy, weak interaction due to low reaction cross-sections, isotope sensitivity, etc., of neutron scattering result in an excellent non-destructive tool for probing environmentally isolated electrochemical energy storage systems. Besides neutron diffraction, which is the most widely used neutron scattering technique in battery research, there is a number of different neutron-based methods capable of delivering unique information about the processes occurring in lithium-ion batteries on various length scales, e.g., neutron imaging,<sup>[11,12]</sup> small-angle neutron scattering,<sup>[13]</sup> quasi-elastic neutron scattering,<sup>[14]</sup> reflectometry,<sup>[15]</sup> neutron depth profiling,<sup>[16]</sup> positron annihilation spectroscopy,<sup>[17]</sup> neutron-induced prompt gamma activation analysis.<sup>[18]</sup>

In the current contribution we apply spatially resolved neutron powder diffraction. The aim of the current work is multidirectional and consists of several subtasks:

- 1) Extension of the results for the non-destructive quantification of lithium electrolyte and studies of its distribution reported in ref. [9] to intermediate states-of-fatigue and drawing correlations with residual capacities.
- 2) Correlating the increasing internal cell resistance, which inhibits an increase of the resistive heating during cycling, to the temperature distribution on the cell surface.

- 3) Comparison of the results on electrolyte subsystem obtained with neutron scattering and calorimetry, demonstrates to be a powerful tool for quantification of liquid electrolyte by the analysis of the thermodynamic response from the battery.<sup>[19]</sup>

A series of experiments applying neutron diffraction, differential thermal analysis (DTA), non-contacting temperature sensing using infrared measurements along with a series of gas chromatography-mass spectroscopy for characterizations of electrolyte composition similar to these reported in ref. [20] was applied for characterization of cells with different stabilized fatigue states.

## 2. Results and Discussion

### 2.1. Average Aging Behavior

As already mentioned, the batch of cells previously reported in ref. [9] was studied. With increasing cycle number, the cells display at first a continuous and later on a nonlinear capacity loss (Figure 1a): at cycle numbers below  $\approx 550$ , the observed cell capacity loss can be well approximated by a  $\sqrt{\text{time}}$  behavior (Figure S1, Supporting Information) and at cycle numbers above 550–600 cycles an accelerated capacity loss occurs, which is referred to the saturation stage in literature.<sup>[21]</sup> The observed cell aging was supplemented by the increase of cell resistance, which is commonly believed to be responsible for a minimum on the voltage curve at the initial stage of cell discharge (Figure 1b).

An increasing cell resistance (Figure S2, Supporting Information) directly leads to increased resistive heating of cell components, which can result in an accelerated drying out of the cell, consumption of electrolyte additives/modifications of the electrolyte content, side reactions on the electrodes, uncontrolled formation of passivation layers, etc. The electrode stack in lithium-ion cells is characterized as a poor and anisotropic heat conductor making its experimental and theoretical characterization not trivial. Degree of complexity often rises with the increase of cell dimensions or with sophisticated layouts. Temperature sensing of electrochemical cells is an actively developing method in battery research, whose relation to cell lifetime, performance and aging is highly relevant and still needs to be further explored.

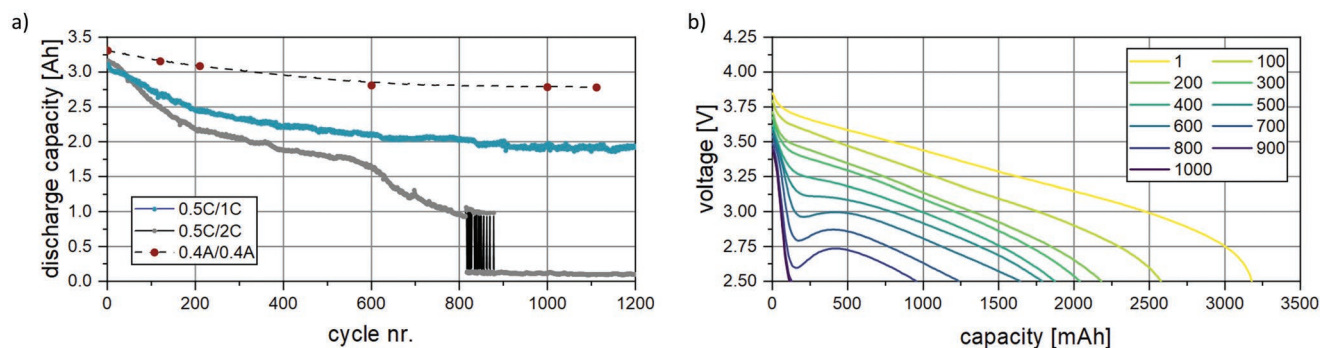


**Figure 1.** a) Evolution of cell capacity for selected cylinder-type cells cycled using 0.5 C/1 C, 0.5 C/2 C, and 0.4 A; b) discharge voltage profile versus cell capacity for various cycles of the selected cell.

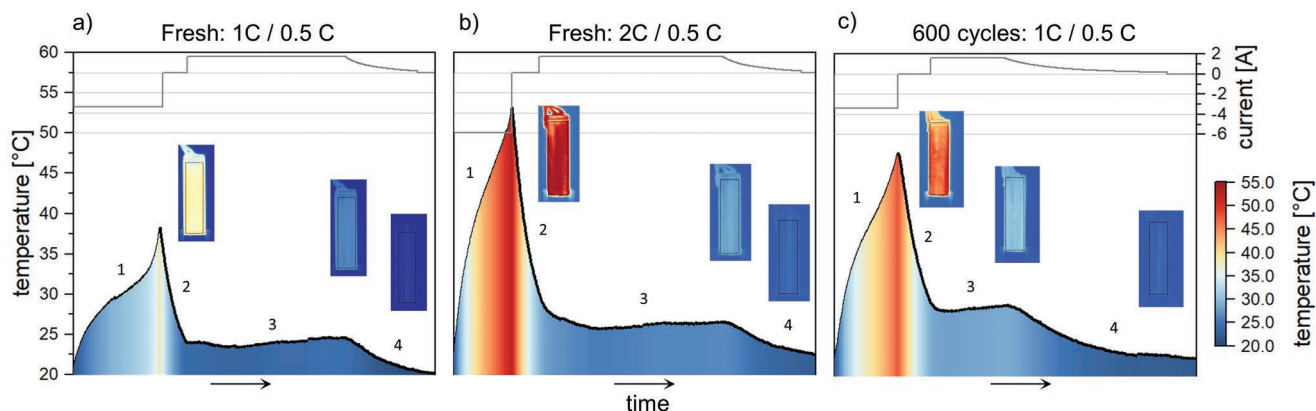


**Figure 2.** Average surface temperature of selected 18650-type cells versus cell discharge (CV)/charge (CCCV, 0.5 C, C/10 CV cutoff). Gray line corresponds to applied charge/discharge current, black line, and colored area indicate the average cell temperature. Sections 1–4 correspond to charge and discharge regions. Selected 2D temperature distributions are depicted at transitions from 1 to 2, 3 to 4 and at the end of phase 4. Refer to Supporting Information for 2D distribution of temperatures.

Recently several different concepts were proposed to probe the cell temperature in the interior of the electrode stack,<sup>[22,23]</sup> which, however, require a violation of the cell integrity. Alternatively, thermal (infrared) imaging can be used for probing the temperature distribution on the cell surface. Indeed due to poor heat conductivity a slight underestimation up to some percent of the real cell temperature in the cell inner by temperature sensing on the cell surface needs to be expected,<sup>[22]</sup> which, however, can be neglected on the qualitative level or minimized by the usage of low current rates.

Analysis of the temperature profiles on the cell surface of fresh and aged cells indicates substantial differences in dependence of the applied current and cell aging. The portion of the cell electrical power  $I^2R\Delta t$ , where  $I$  is the applied current,  $R$  the ohmic resistance, and  $\Delta t$  the time, will be transformed into cell heating  $mC_p\Delta T$  with  $m$  the mass of the cell,  $C_p$  the heat capacity, and  $\Delta T$  the temperature difference. Typical temperature profile of the cell surface temperature is plotted in **Figure 2**. Measurements started in fully charged state. A rapid increase of the temperature upon cell discharge occurs in the region marked as 1 in **Figure 2a–c**. Increasing the discharge current from 1 C (**Figure 2a**) to 2 C (**Figure 2b**) resulted in a substantially steeper rise in the temperature of the cell surfaces. A similar behavior was observed by Tranter et al.<sup>[24]</sup> Cell aging has been found to contribute to Joule heating as well: discharging the aged cell using 1 C current results in a temperature rise exceeding the temperature rise for the fresh cell discharged with the same current by  $\approx 40\%$ . For comparison the temperature rise of the cell charged with the maximally allowed current<sup>[25]</sup> of nearly 2 C exceeds the temperature rise with 1 C by  $\approx 66\%$ . This can be directly attributed to the increased ohmic resistance of the cell. One can draw certain correlations between the surface temperature and power fading, which, however, would require more systematic and detailed studies off the main scope of the current manuscript.

The temperature of all studied cells is increased in the whole course of the CC cell discharge (region 1 in **Figure 2a–c**). Switching off the discharge current resulted in a nonlinear cell cooling (region 2 in **Figure 2a–c**). Approximation of the cooling profiles using a first-order exponential decay<sup>[26]</sup> yielded the time

constants  $t_2$  listed in **Table 1**. Subsequent cell charging with a moderate applied current of 0.5 C results in slight heating of the cell surface by  $\approx 4–6$  °C above room temperature (region 3 in **Figure 2a–c**): 4.6 °C (1 C) and 4.0 °C (2 C) was noticed for the fresh cells (**Figure 2a–c**), while the aged cell was heated up by 6.7 °C above room temperature during charging. The significant increased heating of the aged cell in comparison to the similar heating of the fresh cell at the same applied current can again be attributed to an increased cell resistance of the aged cell.

The nonlinear character of the temperature evolution of the studied cells during charging has been found similar to the time derivatives of the cell potential  $dU/dt$  (see **Figure S3**, Supporting Information). Further analysis of region 4 in **Figure 2a–c** corresponding to the CV range of CCCV charging needs to be considered along with non-linear decay of current. Two time-constants, namely  $t_4^a$  and  $t_4^b$  (listed in **Table 1**), were needed to describe the reduction of the current in the CV phase of studied cells. In contrast to discharge current, the corresponding cooling profiles (reflecting the decay of mean surface temperature in CV state) can be fitted using a first-order exponential decay with time constant  $t_4$ . Different character/magnitude of time constants during the current ( $t_4^a$  and  $t_4^b$ ) and temperature ( $t_4$ ) relaxations need to be explicitly mentioned, where it can be attributed to a complex interplay between heat relaxation at one side and heat dissipation at the other.

In general, the time constants of the current relaxation collected via either electric or thermal channel have been found nearly identical for the fresh cell independent from the applied current. In contrast, cell aging leads to substantially longer

**Table 1.** Time constants of current and heat relaxation for studied 18650-type cells.

	Fresh [1 C/0.5 C]	Fresh [2 C/0.5 C]	Aged (600 cycles) [1 C/0.5 C]
$t_2$ [s]	642 ± 6	617 ± 4	833 ± 23
$t_4^a$ [s]	220 ± 6	190 ± 6	937 ± 3
$t_4^b$ [s]	1352 ± 4	1289 ± 3	3107 ± 14
$t_4$ [s]	1673 ± 20	1426 ± 19	1704 ± 21

relaxation times. This could be explained with drying out of the aged cell,<sup>[27,28]</sup> where liquid electrolyte reacts to solid side products like the solid electrolyte interphase, which are believed to have a lower thermal conductivity than the pristine liquid electrolyte. The thermal gradients in the 18650-type cells are known to be strongly non-uniform in radial direction.<sup>[29]</sup> Inhomogeneous temperature profiles have also been found at the surface of the studied cells (see Supporting Information Section), where the temperature maximum is observed in the region of cell electrode roll and not at the current lid connection point.<sup>[30]</sup> The degree of temperature uniformity (estimated from the histogram of the experimental distributions, Figure S4, Supporting Information) is proportional to the non-equilibrium cell temperature. However, at high temperatures instead of smooth Gaussian-like histograms, discrete “wings” have been observed attributed to local temperature non-uniformities. More deeper/detailed treatment of the data obtained on the thermal channel was sufficiently limited by the accuracy of the thermal imaging setup, i.e., the magnitude of observed effects has been found comparable to the accuracy of the used instrument.

Summing up, the measured cell surface temperature is tightly related to the increase of the resistive components, which in their turn can be caused by a variety of factors and effects supplementing and inhibiting cell aging.<sup>[6,31]</sup> As recently shown,<sup>[32]</sup> the thermal conductivity of the cell components is affected by different factors, e.g., electrolyte wetting, state-of-health, etc.<sup>[32]</sup> On the other hand, the temperature distribution at the extremum point (transition 1–2, at the vicinity of SOC 100 state), recently reported for a series of pouch bag cells<sup>[33]</sup> have been found very similar to the lithium distribution in the graphite anode<sup>[34,35]</sup> determined using X-ray diffraction radiography. Degree and uniformity of such lithium distribution has been found seriously affected by cell aging,<sup>[27,36,37]</sup> which can also take place for temperature surface profile.

## 2.2. Spatial In-Plane Distribution of Lithium and Electrolyte versus Cell Degradation

The previously reported lithium distributions for a fresh and 600 times cycled cell were extended by experimental data for cells cycled 120, 210, 1000, and 1112 times.<sup>[9]</sup> Experimentally determined in-plane lithium concentrations at middle height for the set of studied cells is plotted in Figure 3. Besides the cell housing and center pin, the in-plane lithium profile in the graphite anode is primarily defined by the cell layout,<sup>[9,36]</sup> i.e., positions of current tabs, where the positive one is located in the middle of the electrode strip, while the negative one is attached at the outer electrode end. In the regions where the current lids are located, the lithium concentrations are reduced due to a lack of active material. Lithium content in these regions is also smeared out due to a relatively coarse resolution of the spatially resolved neutron powder diffraction setup.

A systematic reduction of average lithium content in the fully charged anode with increased cycle number can be stated from Figure 3. Application of the distribution histogram analysis (similar to this reported in refs. [34,35,37]) enabled an unambiguous estimate of relevant distribution parameters. For example, the position of the peak in the histograms corresponds to the

plateau concentration, and its width indicates the distribution quality while the fraction of the peak area over the total histogram area points on the degree of homogeneity. A clear shift of the peak position toward lower lithium concentrations with increased cycle number (Figure S5, Supporting Information) can directly be associated with the loss of active lithium in the studied cells. Further, the observed increase of peak width reflects the reduction of plateau quality with increased cell aging.

The electrolyte distribution in the battery was extracted using the intensity of the characteristic electrolyte peak in frozen state, which appears around 27°–28° in  $2\theta$  at low temperatures.<sup>[9]</sup> Electrolyte concentration maps were constructed for the series of studied cells using a color legend similar to the anode lithiation and are shown in Figure 4 along with the histograms of the distributions. Systematically higher electrolyte concentrations were observed on the outer cell regions, while reduced amounts typically have been found toward the cell center. This is in line with the distribution of compression in radial direction,<sup>[38]</sup> where systematically lower compressions are observed at the outer cell region. The separator is reported to be affected by compression at most, which, taking into account the sponge-like behavior of the jellyroll,<sup>[27]</sup> can explain the preferred localization of the electrolyte in these areas.

Direct analysis of correlations between electrolyte and lithium concentration was unsuccessful: the obtained electrolyte maps cannot be associated vis-à-vis with the previously established picture of electrolyte losses versus lithium losses.<sup>[9]</sup> An adequate explanation of the observed distribution requires taking liquid flow into consideration and analyzing the data collection procedure in detail:

- 1) Studied cells were cycled and measured in a vertical configuration, i.e., with the cylinder axis pointing in the vertical direction.
- 2) During cell cycling, a redistribution of electrolyte takes place, i.e., cell charge causes the excess liquid electrolyte to be pressed out of the separator and electrode stack due to expansion of the negative electrode material;<sup>[27]</sup> cell discharge reverses the process.

At the end of the CC charging process, characterized by the maximum expansion of the cell housing and, correspondingly, the jellyroll, the electrolyte is pressed out of the jellyroll either toward the cell housing or empty electrode-free spaces at the cell top and bottom.<sup>[39]</sup> During the times of the CV phase and the relaxation in the rest phase, the electrolyte flows down, what shows the relevance of the cell cycling position and gravitational forces for battery characterization.<sup>[40]</sup> Here, cell charge forms a metastable state supplemented by relaxation of voltage, pressure and lithium concentration in electrodes along with the relaxation of electrolyte distribution in the battery jellyroll. The shape and magnitude of the electrolyte distribution will depend on different factors like compression and thermal gradients, amount of electrolyte and its viscosity, cell layout, the morphology, porosity and tortuosity of battery components, time, etc. In the current case, where a batch of structurally and chemically identical cells is analyzed, the correct assignment of data would require considering the time variable reflecting the electrolyte transfer. And indeed, replotting the observed

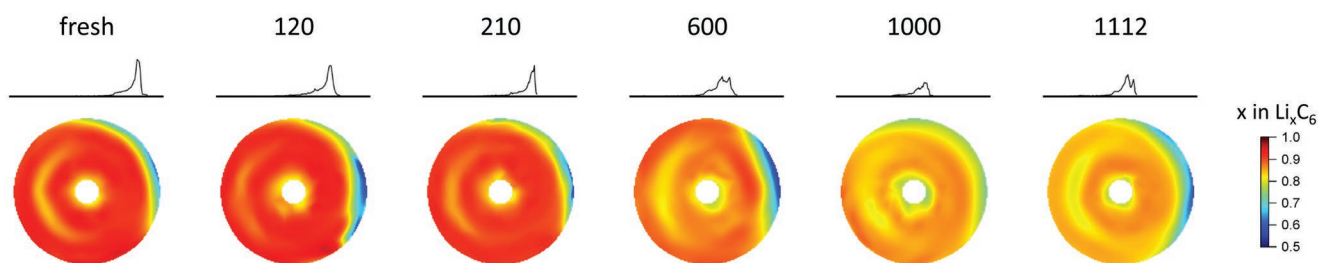


**Figure 3.** In-plane lithium distribution in the graphite anode versus cycle number with collected data in the middle-plane of an 18650-type cell in fully charged state and a temperature of 150 K during data collection. Lithium concentrations are presented in false colors; insets illustrate the distribution histograms.

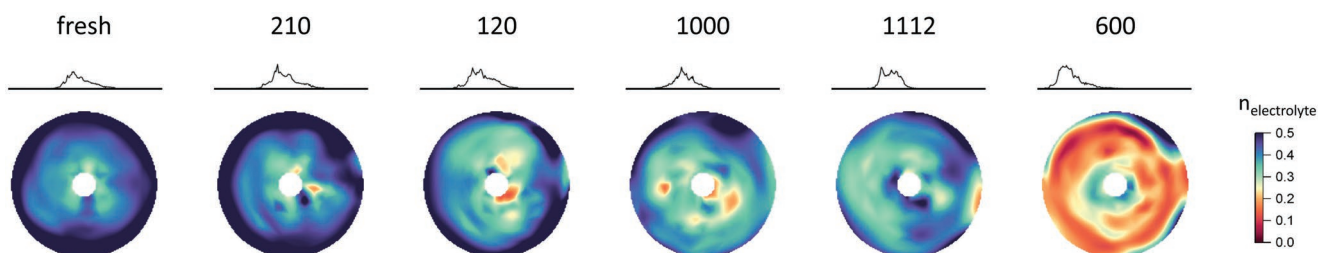


**Figure 4.** In-plane electrolyte distribution determined in the middle plane of 18650-type cell, with color-coded electrolyte content. Insets highlight the distribution histograms. Note that the order of “cycle numbers” is different to Figure 3.

distribution as a function of cell storage time (the time from completing of charge process till data collection) forms a clear trend (Figure 4, from left to right), indicating a continuous behavior for mean in-plane electrolyte distribution in agreement with the one obtained using volume-averaged neutron diffraction.<sup>[9]</sup>

### 2.3. Low Temperature Calorimetry Studies on 18650-Type Cells

Besides the time dependence of electrolyte kinetics, the cycling temperature and the temperature, at which the snapshots were taken, must also be considered as they determine the initial state of the cell. Instead of a rather expensive and labor-intensive neutron diffraction experiment, a relatively simple and straightforward method for quantification of liquid electrolytes using calorimetry was proposed.<sup>[19]</sup> From the thermodynamical point of view, freezing and melting of the liquid electrolyte is a first-order phase transition. It exhibits a thermodynamic signal of exothermic character upon freezing and an endothermic character upon melting, which, in turn, can be used for non-destructive quantification of electrolyte and control of its composition. In this work only the signal upon heating was analyzed in detail as this is enough for characterizing this reversible process. The thermodynamic signal typically has a form of one or several  $\lambda$ -peaks, where the onset temperature of the peak contains information about the phase composition, which is connected to the melting temperature, whereas its intensity/area corresponds to the enthalpy and, correspondingly, to the quantity.<sup>[19]</sup> The method has been successfully validated and found well suited for non-invasive investigations of the electrolyte in lithium-ion batteries.<sup>[41]</sup>

In the current work, an adapted calorimetry measurement utilizing a closed-cycle refrigerator filled with 1 bar He (class 4 purity) as a calorimeter was applied for studies of parts of the variously aged lithium-ion cells described above. An illustration of the data reduction procedure is given in Figure S6 (Supporting Information). The obtained differential thermal signals (DTS) versus cycle number are presented in Figure 4a.<sup>[42]</sup> For the fresh and weakly aged cells, two peaks in the DTS are present: at  $\approx 245$  K (marked as S) and  $\approx 260$  K (marked as L). With increasing cell age, the intensity/signal of the S peak in the DTS is continuously decreasing and vanishes at an aging level corresponding to  $\approx 600$  cycles. Simultaneously, the L peak displays a continuous shift from  $\approx 260$  to 270 K, where it stabilizes after 600 cycles.

Referring to the phase diagrams of the binary carbonates or  $\text{LiPF}_6$ +DMC mixture,<sup>[43–45]</sup> the observed behavior could be attributed to a shift in the composition, where some components of the mixture are preferably consumed during cell operation compared to others. It is worth noting that the used binary phase diagram is a rather crude approximation, which generally neglects the effect of lithium salt and the composition of electrolytes in commercial lithium-ion batteries, which can be highly complex.<sup>[46]</sup>

### 2.4. Gas and Ion Chromatography-Based Characterization of Harvested Electrolyte

The qualitative ex situ analysis of liquid electrolytes extracted from differently aged cells yields certain deviations in the electrolyte composition. The base electrolyte has been found to be a ternary solution consisting of the linear solvents dimethyl

carbonate (DMC), ethyl methyl carbonate (EMC) and the cyclic solvent ethylene carbonate (EC). Furthermore, fluoroethylene carbonate (FEC) was detectable after SPME preconcentration, but below the limits of quantifications for GC-FID.

As electrolyte aging related species, traces of diethyl carbonate (DEC) (According to Ref. [47] DMC/EMC – based electrolytes are known to form DEC via a transesterification reaction of EMC. Low – observed amount of DEC indicates the use of at-least one film-forming electrolyte additive.<sup>[20]</sup>) and selected carbonate-based aging products (2,5-dioxahexanedioic acid dimethyl ester (DMDOHC), ethyl methyl-2,5-dioxahexane dicarboxylate (EMDOHC), butyl methyl carbonate (BMC) and *sec*-butyl methyl carbonate (sBMC)) were detected. DEC and DMDOHC were detectable for each of the three cells, while BMC, sBMC and EMDOHC were present solely in the long-term aged cells. In literature, the presence of these compounds was attributed to EC decomposition reactions, especially during the formation of the solid-electrolyte interphase.<sup>[48,49]</sup> Presumably, the initially preferred FEC consumption during cell formation suppressed the significant formation of EC-based decomposition species. Only after consumption of FEC and ongoing electrolyte decomposition during long-term cycling, these species were formed and detectable.

For the quantitative investigations, no direct correlation between solvent concentration and cell aging was found (Figure 5b), i.e., the average weight ratio DMC:EMC:EC can be written as 72.00(±1.87) : 4.90(±0.24) : 23.11(±0.60). The high DMC/EMC ratio in the solvent mixture determines its low viscosity,<sup>[20]</sup> which is in line with the observed slow electrolyte flow off in the neutron experiment.

The rather static ratio of the electrolyte solvents in combination with the observed low concentrations of its decomposition products<sup>[20,50]</sup> cannot sufficiently explain the obtained evolution of the DTS (Figure 5a). Besides the electrolyte solvents, the conducting LiPF<sub>6</sub> salt used in this case is another possible source of decomposition, which potentially can create a very wide variety of decomposition products. The decomposition of the hexafluorophosphate PF<sub>6</sub><sup>-</sup> anion is promoted through its

reaction with water impurities,<sup>[51]</sup> where a number of potentially hazardous organo (fluoro) phosphates can be formed, also having a negative impact on the environment. In this study, the concentration of PF<sub>6</sub><sup>-</sup> anions was determined for three cells with different aging states: i) fresh/initial state, ii) after 120 cycles, iii) after 1112 cycles. The obtained concentrations are plotted in Figure 5c. In contrast to the solvent mixture, which was found unimpeded of cell aging duration, the concentration of the PF<sub>6</sub><sup>-</sup> anion displayed a clearly decreasing trend with the increasing number of cycles, which is directly correlated to the cycle number (Figure S7, Supporting Information).

## 2.5. Low-Temperature Calorimetry Studies on Synthetic Electrolyte

As shown exemplary for a mixture of LiPF<sub>6</sub> and DMC,<sup>[44]</sup> the conducting salt can strongly affect the form of the DTS. In order to prove this behavior in the current study, a series of electrolyte compositions with fixed DMC:EMC:EC ratio (corresponding to the concentration established for cells in the current study) and various concentrations of LiPF<sub>6</sub> salt was prepared.

Calorimetric studies similar to these carried out for the set of 18650-type cells were performed on the prepared electrolyte compositions. The evolution of the obtained thermodynamic signal upon heating and with subtracted background is plotted in Figure 5d. At higher lithium salt concentrations, the thermal signals of the prepared solution and the lithium-ion batteries were similar in terms of qualitative shape, which can be seen from the S and L peak in Figure 5a,d. At conducting salt concentrations lower than 0.65 m LiPF<sub>6</sub>, an additional  $\lambda$ -type feature on DTS marked as T arises in the electrolyte data in the form of a low-temperature tail next to peak L. The appearance of an additional thermal signal in the studied temperature range could possibly result from a concentration-driven phase transition in the frozen electrolyte occurring in the LiPF<sub>6</sub>- diluted region just below the melting point. Since only one low-intensity peak of the electrolyte

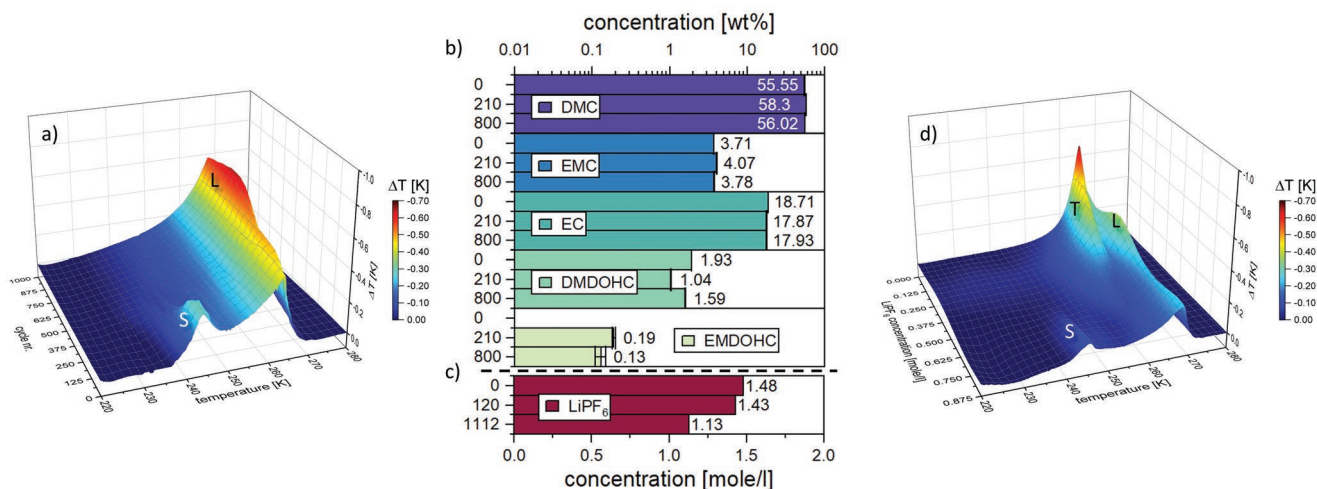


**Figure 5.** a) Calorimetry measurements (differential thermal signal) of differently aged 18650-type cylindrical Li-ion cells, b) chemical content of electrolyte solvents and selected decomposition products (see Supporting Information), c) concentration of LiPF<sub>6</sub> conducting salt and d) calorimetry measurements on synthetic electrolyte mixture with different LiPF<sub>6</sub> concentrations.

was monitored in the resolution-limited diffraction data, no clear conclusion about phase stability can be made from diffraction.

The thermal width of the existence range for the observed intermediate phase is narrowing with the reduction of conducting salt from  $\approx 7$  K at 0.5 M LiPF<sub>6</sub> down to 5 K at 0.2 M LiPF<sub>6</sub> and gets undetectable when the conduction salt concentration approaches zero. Potentially the single L peak seen in the DTS of the fully assembled battery is actually the combined signal of the T and L peak seen in the data of the solvent mixture. This smearing out of the peaks can be attributed to the severe mass difference between the whole battery at one side and a total amount of electrolyte on the other. Based on this one can assume the shift of the T peak toward higher temperatures in the electrolyte solution to be the part of the observed shift of the L peak in the battery data.

The aging-driven electrolyte degradation in the studied cells is reflected by the decomposition of conducting salt. The loss of conducting salt (23.6%) has been found comparable to the loss of the lithium inventory (16.3%) and loss of discharge capacity (15%) when charged with low current. Lowering the LiPF<sub>6</sub> conducting salt concentration is reported to have dramatic effects on the cell performance using EC- and EMC-based electrolyte mixtures,<sup>[52]</sup> leading to higher charge transfer resistances at both electrode sides. In ref. [53], a salt decomposition coupled to EC dehydrogenation was observed, which, however, is expected with a higher probability after cycling at higher temperatures.<sup>[54]</sup>

### 3. Conclusion

A combined approach to analyze and study the fading of the lithium and electrolyte distribution along with the aging driven electrolyte degradation was applied. Thermal imaging performed on three selected examples revealed the temperature on the cell surface proportional to the electric cell power, charge/discharge current and the state-of-fatigue via the increased ohmic resistance. The decay constants of time and heat relaxation have been found unaffected by the applied current but proportional to the aging state of the cells. Non-uniformities of the surface temperature profiles of studied cells were revealed by distribution histograms, where the non-stochastic (systematic) character of the observed non-uniformities may be of interest for future characterizations.

Non-destructive determination of in-plane lithium and electrolyte distribution was performed using spatially resolved neutron powder diffraction in fully charged state at low temperatures. A systematic reduction of lithium concentration in the graphite anode with increasing cycle number and the corresponding degree of cell fatigue was observed. This decrease is attributed to the loss of free lithium inventory, which is in turn proportional to the cell discharge capacity loss. In general, the 2D lithium distribution in the graphite turns less uniform with increased level of fatigue, which is reflected in the deviations of lithium concentrations from the plateau-like behavior. In addition to the loss of mobile lithium inventory, a loss of electrolyte takes place. An accurate correlation of in-plane lithium

and electrolyte concentrations was complicated by the time-dependent flow of the liquid electrolyte.

A calorimetry-based characterization of the electrolyte sub-system was performed by monitoring the thermodynamic response of 18650-type cells in the temperature range of the freezing of the electrolyte. Besides the loss of electrolyte, the evolution of the obtained endothermic thermal signals versus stabilized state of fatigue/health revealed the chemical degradation of electrolyte. The chemical analysis of the electrolyte solutions, which were extracted from aged cells, yields the stability of the solvent mixture to 72.00(±1.87) : 4.90(±0.24) : 23.11(±0.60) DMC:EMC:EC ratio within the applied study. Typical electrolyte decomposition products have been found to be present in small amounts, which are not critical for cell performance. Instead, the concentration of conducting salt LiPF<sub>6</sub> has been found to be reduced by  $\approx 25\%$  during cycling from the fresh state (1.48 mol L<sup>-1</sup>) to 1000 cycles (1.13 mol L<sup>-1</sup>). Lowering the LiPF<sub>6</sub> concentration leads to an increasing charge transfer resistance, resulting in power fade and cell failure through resistive heating. DTA studies on synthetic electrolyte mixtures adopting the above-mentioned DMC:EMC:EC ratio with different concentrations of LiPF<sub>6</sub> conducting salt revealed a qualitatively similar picture to this obtained from the investigated 18650-type cells. The observed concentration-dependent discrepancies can be attributed to electrolyte non-uniformities, for example, in the form of a stratification effect known from lead-acid batteries.<sup>[55]</sup>

The performed studies yielded an interesting correlation between loss of lithium inventory and decomposition of lithium salt in the electrolyte. Both values have been found decreasing in a similar manner and with similar magnitude in the course of extensive cycling. The observed correlation opens an interesting perspective toward improvement of battery lifetime and cycling stability by the introduction of an artificial lithium source. Currently, the usage of overlithiated NCMs and other lithium-rich compounds is discussed in the literature as a realistic way to maintain the lithium inventory constant (or minimize its losses) during the formation process. Considering extensive battery cycling, an alternative way to keep the lithium inventory stable can be potentially introduced by controlling the lithium concentration in the electrolyte. This in turn will stabilize the amount of movable lithium between the electrodes. It can be realized in various ways, the simplest being the introduction of a slowly dissolving form/modification of lithium salt into the battery.

It is worth to note that very similar DTA signals were obtained for a series of different cylinder-type cells adopting different cell chemistries and therefore varying compositions of solvents as electrolyte (see Figure S8, Supporting Information) generally indicating a similar thermodynamic behavior of batteries in this region. Besides the NCR18650B a vanishing of the S-type signal in DTA data was also observed for aged NCR18650GA cells (unpublished). More complex changes have been found between differently aged APR18650 M1-A (unpublished) cells. In general, the structure of solvents and electrolyte mixtures needs to be studied more systematically and more detailed, as it contains a wide variety of different possible structures and properties directly affecting the cell stability and performance.

## 4. Experimental Section

A set of commercially available NCR18650B cells based on NCA|C cell chemistry and having a nominal capacity of 3.4 Ah was studied. The detailed cell cycling procedure is reported in ref. [9]. The spatially resolved neutron powder diffraction experiment was carried out at the materials science diffractometer STRESS-SPEC (FRM II, Garching b. München, Germany).<sup>[56]</sup> The experimental procedure followed the reported procedure in ref. [57]. For determination of the cell layout in the investigated cell type the X-ray computed tomography studies were carried out using a phoenix v|tome|x s 240 tomography scanner (General Electric).

Contactless temperature measurements on the surface of selected cells were performed using an infrared camera FLIR T335. Reported calorimetry studies were performed using a closed-cycle refrigerator available as the standard sample environment at the powder diffractometer SPODI.<sup>[58]</sup> Liquid electrolytes were harvested from the electrode stack through centrifugation. Ion chromatography (IC) with conductivity detection (CD), quantitative gas chromatography-flame ionization detector (GC-FID) experiments and qualitative gas chromatography-mass spectrometry (GC-MS) were performed on the extracted electrolyte. All experiments are reported in detail in the Supplementary Information section.

## Supporting Information

Supporting Information is available from the Wiley Online Library or from the author.

## Acknowledgements

The authors gratefully acknowledge the financial support provided by the Heinz Maier-Leibnitz Zentrum (Technische Universität München), German Federal Ministry of Education and Research (BMBF project 05K16VK2 and 05K19VK3), and Bavaria California Technology Center (BaCaTeC, project 14[2014-02]). They thank the Heinz Maier-Leibnitz Zentrum for the provision of beamtime and access to their infrastructure. The authors wish to thank J. Pfanzelt (MLZ) for the assistance with infrared camera measurements.

Open access funding enabled and organized by Projekt DEAL.

## Conflict of Interest

The authors declare no conflict of interest.

## Data Availability Statement

The data that support the findings of this study are available from the corresponding author upon reasonable request.

## Keywords

aging, conducting lithium salt, differential thermal analysis, electrolyte compositions, lithium-ion batteries, neutron powder diffraction

Received: May 13, 2022

Revised: August 1, 2022

Published online: September 30, 2022

- [1] A. Wang, S. Kadam, H. Li, S. Shi, Y. Qi, *npj Comput. Mater.* **2018**, *4*, 15.
- [2] Q. Wang, L. Jiang, Y. Yu, J. Sun, *Nano Energy* **2019**, *55*, 93.
- [3] C. Pfaffenhuber, M. Göbel, J. Popovic, J. Maier, *Phys. Chem. Chem. Phys.* **2013**, *15*, 18318.
- [4] Q. Li, J. Chen, L. Fan, X. Kong, Y. Lu, *Green Energy Environ.* **2016**, *1*, 18.
- [5] Y.-S. Hu, Y. Lu, *ACS Energy Lett.* **2020**, *5*, 3633.
- [6] C. R. Birkel, M. R. Roberts, E. McTurk, P. G. Bruce, D. A. Howey, *J. Power Sources* **2017**, *341*, 373.
- [7] M. M. Kabir, D. E. Demirocak, *Int. J. Energy Res.* **2017**, *41*, 1963.
- [8] D. Beck, P. Dechent, M. Junker, D. U. Sauer, M. Dubarry, *Energies* **2021**, *14*, 3276.
- [9] M. J. Mühlbauer, D. Petz, V. Baran, O. Dolotko, M. Hofmann, R. Kostecky, A. Senyshyn, *J. Power Sources* **2020**, *475*, 228690.
- [10] A. Senyshyn, M. J. Mühlbauer, O. Dolotko, H. Ehrenberg, *J. Power Sources* **2015**, *282*, 235.
- [11] R. F. Ziesche, T. Arlt, D. P. Finegan, T. M. M. Heenan, A. Tengattini, D. Baum, N. Kardjilov, H. Markötter, I. Manke, W. Kockelmann, D. J. L. Brett, P. R. Shearing, *Nat. Commun.* **2020**, *11*, 777.
- [12] A. Senyshyn, M. J. Mühlbauer, K. Nikolowski, T. Pirling, H. Ehrenberg, *J. Power Sources* **2012**, *203*, 126.
- [13] S. Seidlmayer, J. Hattendorff, I. Buchberger, L. Karge, H. A. Gasteiger, R. Gilles, *J. Electrochem. Soc.* **2015**, *162*, A3116.
- [14] C.-W. Hu, C.-H. Lee, P.-J. Wu, *J. Chin. Chem. Soc.* **2021**, *68*, 507.
- [15] J. E. Owejan, J. P. Owejan, S. C. DeCaluwe, J. A. Dura, *Chem. Mater.* **2012**, *24*, 2133.
- [16] S. C. Nagpure, R. G. Downing, B. Bhushan, S. S. Babu, L. Cao, *Electrochim. Acta* **2011**, *56*, 4735.
- [17] S. Seidlmayer, I. Buchberger, M. Reiner, T. Gigl, R. Gilles, H. A. Gasteiger, C. Hugenschmidt, *J. Power Sources* **2016**, *336*, 224.
- [18] I. Buchberger, S. Seidlmayer, A. Pokharel, M. Piana, J. Hattendorff, P. Kudejova, R. Gilles, H. A. Gasteiger, *J. Electrochem. Soc.* **2015**, *162*, A2737.
- [19] R. P. Day, J. Xia, R. Petibon, J. Rucska, H. Wang, A. T. B. Wright, J. R. Dahn, *J. Electrochem. Soc.* **2015**, *162*, A2577.
- [20] J. Henschel, F. Horsthemke, Y. P. Stenzel, M. Evertz, S. Girod, C. Lürenbaum, K. Kösters, S. Wiemers-Meyer, M. Winter, S. Nowak, *J. Power Sources* **2020**, *447*, 227370.
- [21] X. Lin, J. Park, L. Liu, Y. Lee, A. M. Sastry, W. Lu, *J. Electrochem. Soc.* **2013**, *160*, A1701.
- [22] J. Huang, L. Albero Blanquer, J. Bonefacino, E. R. Logan, D. Alves Dalla Corte, C. Delacourt, B. M. Gallant, S. T. Boles, J. R. Dahn, H.-Y. Tam, J.-M. Tarascon, *Nat. Energy* **2020**, *5*, 674.
- [23] G. Yang, C. Leitão, Y. Li, J. Pinto, X. Jiang, *Measurement* **2013**, *46*, 3166.
- [24] T. G. Tranter, R. Timms, T. M. M. Heenan, S. G. Marquis, V. Sulzer, A. Jnawali, M. D. R. Kok, C. P. Please, S. J. Chapman, P. R. Shearing, D. J. L. Brett, *J. Electrochem. Soc.* **2020**, *167*, 110538.
- [25] Aged cell (cycled 600 times) displayed an immediate voltage drop from 4.2 to 2.5 V when discharged with 2 C current.
- [26]  $T(t) = T_{\text{offset}} + T_{1 \leftrightarrow 2} \cdot \exp\left(-\frac{(t-t_{1 \leftrightarrow 2})}{t_2}\right)$ , where  $T_{\text{offset}}$  the temperature of the base line,  $T_{1 \leftrightarrow 2}$  the temperature at the end of cell discharge,  $t_{1 \leftrightarrow 2}$  the corresponding time separating regions 1 and 2 and  $t_2$  the time constant of the temperature decay.
- [27] M. J. Mühlbauer, O. Dolotko, M. Hofmann, H. Ehrenberg, A. Senyshyn, *J. Power Sources* **2017**, *348*, 145.
- [28] R. Gauthier, A. Luscombe, T. Bond, M. Bauer, M. Johnson, J. Harlow, A. Louli, J. R. Dahn, *J. Electrochem. Soc.* **2022**, *169*, 020518.
- [29] G. Zhang, L. Cao, S. Ge, C.-Y. Wang, C. E. Shaffer, C. D. Rahn, *J. Electrochem. Soc.* **2014**, *161*, A1499.
- [30] J. B. Robinson, J. A. Darr, D. S. Eastwood, G. Hinds, P. D. Lee, P. R. Shearing, O. O. Taiwo, D. J. L. Brett, *J. Power Sources* **2014**, *252*, 51.



- [31] C. Schlasza, P. Ostertag, D. Chrenko, R. Kriesten, D. Bouquain, 2014 *IEEE Transportation Electrification Conference and Expo (ITEC)*, **2014**, pp. 1–6, <https://doi.org/10.1109/ITEC.2014.6861811>.
- [32] F. Richter, P. J. S. Vie, S. Kjelstrup, O. S. Burheim, *Electrochim. Acta* **2017**, *250*, 228.
- [33] S. Goutam, J.-M. Timmermans, N. Omar, P. Van den Bossche, J. Van, *Mierlo Energies* **2015**, *8*, 8175.
- [34] M. J. Mühlbauer, A. Schökel, M. Etter, V. Baran, A. Senyshyn, *J. Power Sources* **2018**, *403*, 49.
- [35] A. Senyshyn, V. Baran, M. Mühlbauer, M. Etter, M. Schulz, K. Tu, Y. Yang, *ACS Appl. Energy Mater.* **2021**, *4*, 3110.
- [36] D. Petz, M. J. Mühlbauer, V. Baran, M. Frost, A. Schökel, C. Paulmann, Y. Chen, D. Garcés, A. Senyshyn, *J. Power Sources* **2020**, *448*, 227466.
- [37] D. Petz, M. J. Mühlbauer, A. Schökel, K. Achterhold, F. Pfeiffer, T. Pirling, M. Hofmann, A. Senyshyn, *Batteries Supercaps* **2021**, *4*, 327.
- [38] F. Ebert, M. Spielbauer, M. Bruckmoser, M. Lienkamp, *J. Energy Storage* **2022**, *49*, 104143.
- [39] J. Hemmerling, J. Guhathakurta, F. Dettinger, A. Fill, K. P. Birke, *Batteries* **2021**, *7*, 61.
- [40] C. Sauter, R. Zahn, V. Wood, *J. Electrochem. Soc.* **2020**, *167*, 100546.
- [41] L. M. Thompson, J. E. Harlow, A. Eldesoky, M. K. G. Bauer, J. H. Cheng, W. S. Stone, T. Taskovic, C. R. M. McFarlane, J. R. Dahn, *J. Electrochem. Soc.* **2021**, *168*, 020532.
- [42] For the sake of convenience the z-axis in Figure 5 is inverted, i.e., peaks in the graph correspond to endothermic processes.
- [43] M. S. Ding, K. Xu, T. R. Jow, *J. Therm. Anal. Calorim.* **2000**, *62*, 177.
- [44] D. J. Xiong, M. Bauer, L. D. Ellis, T. Hynes, S. Hyatt, D. S. Hall, J. R. Dahn, *J. Electrochem. Soc.* **2018**, *165*, A126.
- [45] M. S. Ding, K. Xu, S. Zhang, T. R. Jow, *J. Electrochem. Soc.* **2001**, *148*, A299.
- [46] E. R. Logan, E. M. Tonita, K. L. Gering, L. Ma, M. K. G. Bauer, J. Li, L. Y. Beaulieu, J. R. Dahn, *J. Electrochem. Soc.* **2018**, *165*, A705.
- [47] H. Yoshida, T. Fukunaga, T. Hazama, M. Terasaki, M. Mizutani, M. Yamachi, *J. Power Sources* **1997**, *68*, 311.
- [48] C. Peschel, F. Horsthemke, M. Leißing, S. Wiemers-Meyer, J. Henschel, M. Winter, S. Nowak, *Batteries Supercaps* **2020**, *3*, 1183.
- [49] F. Horsthemke, A. Friesen, L. Ibing, S. Klein, M. Winter, S. Nowak, *Electrochim. Acta* **2019**, *295*, 401.
- [50] B. L. D. Rinkel, D. S. Hall, I. Temprano, C. P. Grey, *J. Am. Chem. Soc.* **2020**, *142*, 15058.
- [51] C. Schultz, S. Vedder, B. Streipert, M. Winter, S. Nowak, *RSC Adv.* **2017**, *7*, 27853.
- [52] D. J. Xiong, T. Hynes, J. R. Dahn, *J. Electrochem. Soc.* **2017**, *164*, A2089.
- [53] Y. Yu, P. Karayalali, Y. Katayama, L. Giordano, M. Gauthier, F. Maglia, R. Jung, I. Lund, Y. Shao-Horn, *J. Phys. Chem.* **2018**, *122*, 27368.
- [54] M. Metzger, P. Walke, S. Solchenbach, G. Salitra, D. Aurbach, H. A. Gasteiger, *J. Electrochem. Soc.* **2020**, *167*, 160522.
- [55] D. Takamatsu, T. Hirano, A. Yoneyama, T. Kimura, M. Harada, M. Terada, T. Okoshi, *Chem. Commun.* **2020**, *56*, 9553.
- [56] M. Hofmann, R. Schneider, G. A. Seidl, J. Rebelo-Kornmeier, R. C. Wimpory, U. Garbe, H. G. Brokmeier, *Phys. B* **2006**, *385–386*, 1035.
- [57] A. Senyshyn, M. J. Mühlbauer, O. Dolotko, M. Hofmann, H. Ehrenberg, *Sci. Rep.* **2015**, *5*, 18380.
- [58] M. Hoelzel, A. Senyshyn, N. Juenke, H. Boysen, W. Schmahl, H. Fuess, *Nucl. Instrum. Methods Phys. Res., Sect. A* **2012**, *667*, 32.